

JPRS-CST-91-022
12 NOVEMBER 1991



JPRS Report

Science & Technology

China

19980203 304

DISTRIBUTION STATEMENT A

Approved for public release;
Distribution Unlimited

DTIC QUALITY INSPECTED 2

REPRODUCED BY
U.S. DEPARTMENT OF COMMERCE
NATIONAL TECHNICAL
INFORMATION SERVICE
SPRINGFIELD, VA 22161

SCIENCE & TECHNOLOGY
CHINA

CONTENTS

AEROSPACE

- Design, Estimation of Performance Gain for Combined
Extended Nozzle
[Wang Chengxuan; ZHONGGUO KONGJIAN KEXUE JISHU,
No 2, Apr 91]..... 1
- Design of Orificed Hollow Cathode for 8-cm Mercury-Ion
Thruster Prototype
[Zhang Shiliang, Hu Yongnian; ZHONGGUO KONGJIAN
KEXUE JISHU, No 2, Apr 91]..... 11

LASERS, SENSORS, OPTICS

- Theoretical Analysis of Raman Free Electron Laser Experiment
Without Axial Magnetic Field
[Wang Pingshan, Hu Kesong, et al.; WULI XUEBAO [ACTA
PHYSICA SINICA], No 5, May 91]..... 22
- Performances and Possible Uses of Far Infrared Free Electron
Lasers
[R. Coisson, Fu Ensheng; GUANGXUE XUEBAO [ACTA
OPTICA SINICA], No 8, Aug 91]..... 34

Design, Estimation of Performance Gain for Combined Extended Nozzle

92FE0002B Beijing ZHONGGUO KONGJIAN KEXUE JISHU [CHINESE SPACE SCIENCE AND TECHNOLOGY] in Chinese Vol 11 No 2, Apr 91 pp 58-63

[Article by Wang Chengxuan [3769 2052 6513] of Huaihai Institute of Engineering; MS received 10 Oct 90]

[Text] Abstract

This paper describes the design method for an extended nozzle with gas-deployed skirt and double-nested exit cone, and estimates the performance gain of this nozzle. The results show that the nozzle has significant practical value.

I. Introduction

The extended nozzle is a new nozzle design which has been under development over the past 20 years for use on intercontinental [ballistic] missiles and the final stages of space planes; it is generally acknowledged that this new nozzle can significantly increase the range or the payload of the vehicle. The extended nozzles in existence today can be divided into two types. One is a gas-deployed skirt design which resembles a folded umbrella; it is actually a metallic skirt folded along the radial direction toward the inner chamber of the nozzle. Its advantages are: light weight, simple structure, ease of deployment, and pre-seal design; however, its application is rather limited (the area ratio must be greater than 25). The other type is a nested-tube exit cone which can be extended during operation; its design consists of a fixed exit cone (also called the base nozzle) and one or two extension nozzles which can be extended to the designated operating position by an executive mechanism (which may be a rigid or a flexible actuator tube). The nested type extended nozzle is structurally simple, operationally reliable, and has adjustable expansion ratio to provide higher performance gain. But the number of exit cones is limited to a maximum of three. Table 1 shows a comparison of the performance of exit cone between the nested tube design and the gas-deployed skirt design.¹ It is not difficult to see that one can design a superior extended nozzle by incorporating the desirable features and eliminating the shortcomings from each of the above designs.

Table 1. Comparison of the Performance of Exit Cone Between the Nested Tube Design and the Gas-Deployed Skirt Design

Performance criteria Design type	Retraction ability	Thermal structural property	Allowable range	Stability	Continuity of inner surface	Deployment after ignition	Deployment system	Continuous adjustment during flight	Particle collision capability	Tunability	Complexity and reliability
Nested tube design	Good	Very good	No limit (not to exceed 3 exit cones)	Very good	May have steps	Possible	Actor tube	Possible (with 3 exit cones)	Good	Possible	Relatively simple, very good
Gas-deployed skirt design	Good	Good	Area ratio greater than 25	Good	Surface may be non-ideal	Impossible	Gas-operated automatic deployment	Impossible	Good	Impossible	Simple but may be non-ideal

Over the past 10 years, significant progress has been made in this country in the development of extended nozzles.² Both the gas-deployed skirt type nozzles and the nested-tube-type nozzles have been tested, and a technology base has been established for designing a composite type extended nozzle.

II. Design of the Extended Nozzle

1. Design Criteria and Requirements

The design criteria and requirements for the extended nozzle include: operating conditions, engine performance, and weight and spatial constraints. They are discussed below:

- 1) Operating conditions, i.e., the operating altitude and environmental requirements (such as overload, shock, vibration, storage and operating temperature, nuclear radiation environment);
- 2) Separation and operating mode: whether ignition takes place before or after deployment;
- 3) Weight and spatial constraints: the allowable nozzle weight and the space between stages (which determine the retraction length and the radial dimensions of the extended nozzle);
- 4) Engine dimensions, thrust level, combustion-chamber temperature, operating pressure and duration;
- 5) Throat diameter, submerge depth, exit half angle and expansion ratio of the nozzle;
- 6) Deployment length, deployment time and speed;
- 7) Nozzle swivel angle, velocity and acceleration as well as the swivel moment and load position;
- 8) Materials used and their properties;
- 9) Stability and reliability requirements;
- 10) Economy, etc.

2. Practical Design Considerations

An extended nozzle with a gas-deployed skirt and a double-nested-tube design has three segments: a) the base nozzle and the double-nested extendable exit cone (the latter has a metallic skirt which can be folded in the radial direction); b) the deployment system; and c) the power-supply system. The basic principle of this design is to fully take advantage of the results and the mature technologies that have been developed for the gas-deployed skirt and single/double rigid-action swiveling extended nozzles. Figure 1 shows a schematic diagram of the extended nozzle design.

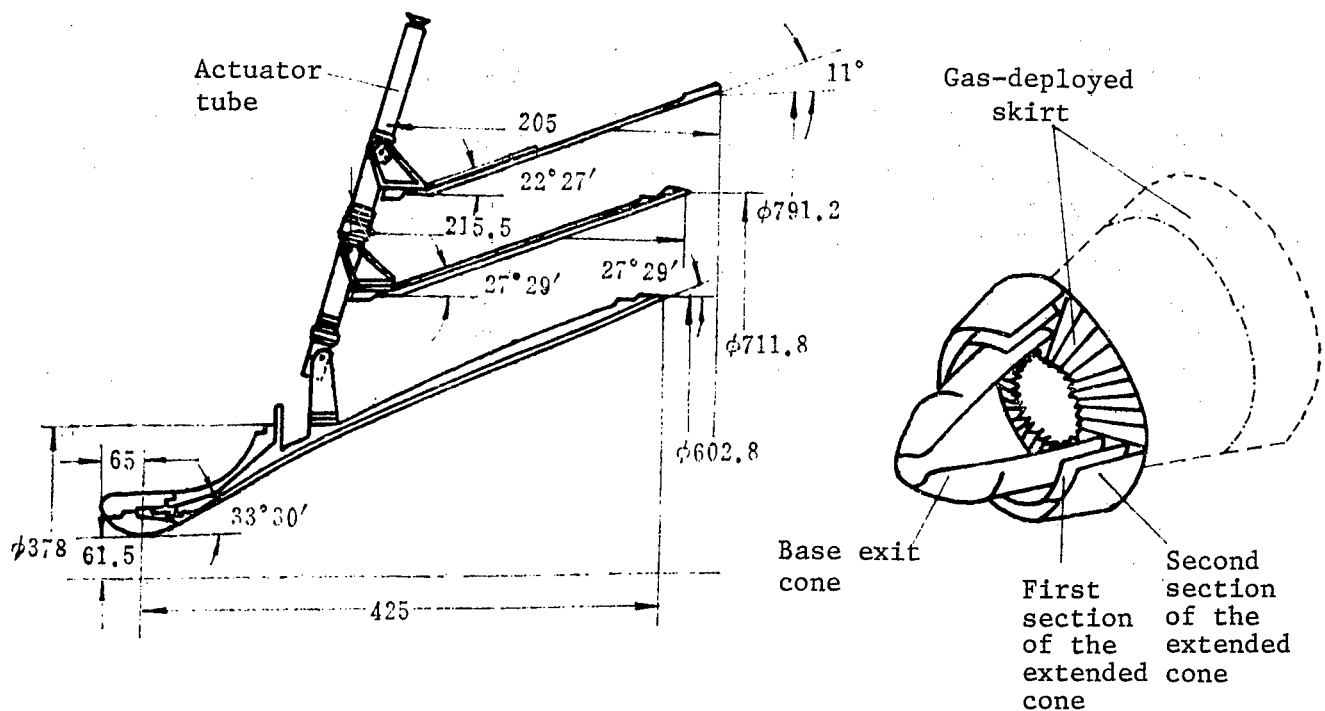


Figure 1. Schematic Diagram of a Composite Extended Nozzle

Some of the practical design issues will be discussed in each of the following areas:

(1) Design of the Base Nozzle and the Extended Exit Cone

1) Determination of the number of exit cones. The number of extended exit cones is determined on the basis of spatial constraints, performance requirements, and the effect on thrust vector control. A double nested exit cone is used in this design.

2) Determination of the length of the exit cone and the exit diameter. A very long base exit cone implies a short extended exit cone whose effectiveness would be limited; on the other hand, a very short base exit cone will result in an excessively long and heavy extended exit cone and significantly increase the weight of the deployment system. Therefore, the length and diameter of the exit cone (including the gas-deployed skirt) must be carefully chosen to keep the expansion ratio relatively small and to keep the exit cone diameter in its retracted position to be less than the engine diameter.

3) Design of the gas-deployed skirt. The metallic skirt is either mechanically attached or bonded to the second section of the extended exit cone, and folded along the radial direction. Clearly, the size of the skirt is constrained by the diameter of the exit cone; however, with careful design, it is possible to have the deployed exit diameter greater than the engine diameter, and to keep the gas-deployed skirt from extending until the movable cone is deployed so that the exhaust gas would not enter. Such a design is particularly desirable on strategic missiles.

4) Design of the inner surface. In order to avoid particle collisions, this design uses a special nozzle with an idealized surface for the throat region and for the entrance section of the exit cone. To satisfy the spatial constraints of the exposed part of the nozzle and to meet the performance gain requirements, the length of the nozzle is chosen to be as short as possible and its expansion ratio is chosen to be as large as possible; also the shape of the nozzle surface is chosen to be a third-order polynomial, as shown in Figure 2. In its fully extended and deployed position, the nozzle length is 1010 mm, and the inner diameter of the nozzle exit is 825.1 mm, the expansion ratio can be as high as 45. For the purpose of comparison, the figure also shows the inner surface of a fixed exit cone with the same exposed length.

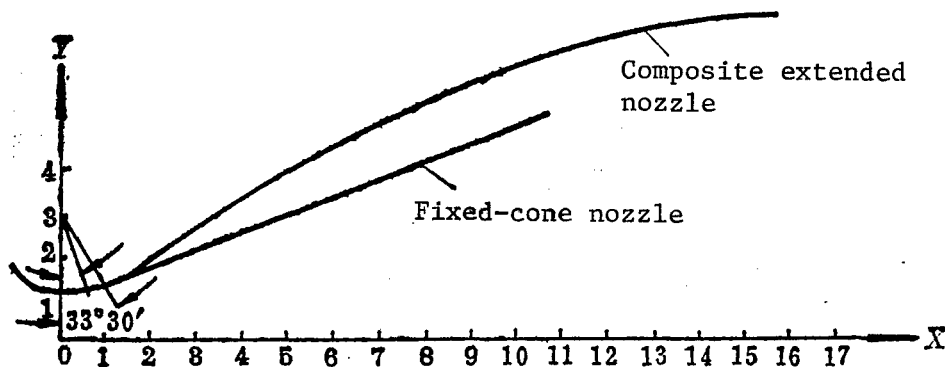


Figure 2. Inner Surface of a Composite Extended Nozzle in Its Fully Extended and Deployed Position

5) Materials for the outer shell and the skirt. The outer shell of the nozzle is made of aluminum alloy; the gas-deployed skirt is made of niobium alloy; in other countries, the skirt is generally made of metallic actinium and stainless steel.³

6) Ablation material for the exit cone. Initially, silicon oxide fiberglass wrapped with cloth tape is used as ablation material; the improved design will use carbon-carbon composite material to reduce the mass of the exit cone.

7) Sealing material. Silicon rubber O-rings are used not only as sealing material but also as a cushion to absorb the impact load.

8) Locking mechanism. A mechanical locking mechanism is used, as in the case of the single-section swiveling extended nozzle.

9) Insulation material. In order to prevent damages caused by gas leaks, it is necessary to coat the actuator tube, the exit cone, the gas-deployed skirt and the support structure with a layer of protective metallic oxide (e.g., aluminum oxide or silicon oxide).

10) Buffer material. Conventional sponge-rubber plates (the improved design will use soft graphite) are used as the buffer material to reduce vibration and to absorb the impact load during deployment.

11) Continuity of the inner surface. Steps or discontinuities at the joints of the exit cone will cause the heat conduction coefficient along the wall downstream of the steps to increase and therefore result in severe ablation of the nozzle. In order to obtain a better surface, these steps must be weakened; however, based on fabrication and assembly considerations, the steps must retain sufficient thickness to avoid defects or damages.

(2) Design of the Deployment System

A complete deployment system should contain the following segments: the positioning and directional guidance segment, the locking unit, the sealing unit and the buffer unit. The primary requirements for a deployment system are: good deployment performance, accurate synchronization, axial symmetry and controllability. In designing the deployment system, one must carry out load calculations which take into account the inertial load and the pre-tension of seal rings, as well as the thrust and aerodynamic load after the nozzle is deployed. Aerodynamic loads must also be calculated in designing the actuator tube. Clearly, the above loads will not occur simultaneously. The initial stage of deployment is dominated by inertial load and aerodynamic load; the final stage of deployment is dominated by the pre-tension and the increased thrust force. For each stage one can determine the maximum load for each of the actuator tubes.

This design uses four nested actuator tubes (a detailed description is presented by the designer in a separate paper). Gas is passed through four equal-length manifolds into the actuator tubes; when the pressure inside the manifold reaches a certain value, the actuator tube becomes pressurized, and begins to extend and rotate. In the deployed configuration, the travel of the first section of the exit cone is 100 mm, and that of the second section is 200 mm. Each actuator tube is equipped with a pulley system to ensure synchronized travel. At the end of the deployment sequence, the mouth of the exit cone is pressed against the cushion and the seal ring, and it is locked in the deployed position by a mechanical locking device. After the nozzle is deployed and before engine cut-off, the pressure and rigidity inside the actuator tube are maintained by the pressure in the manifold.

The metal skirt which is folded along the radial direction is deployed directly by the low-pressure gas from engine ignition, and is stabilized in the open position by the internal aerodynamic pressure of the jet stream from the exhaust nozzle.

(3) Selection of Power Supply

During cold tests and ground tests, the rigid actuator tube is operated by compressed air; however, when conditions permit, it can also be powered by the gas from a gas generator. To develop this new power supply, effort should be initiated to study the design, fabrication and testing of gas generators.

III. Estimation of Performance Gain

The performance gain that is achievable by the extended nozzle can be estimated as follows. First, the performance is calculated based on the expansion ratio; this performance estimate is modified by the additional propellant due to reduction in the submerge depth of the nozzle and the performance degradation caused by the increase in structural weight. If the shockwave loss in the supersonic flow caused by discontinuities of the inner surface is neglected, then the net performance gain of the extended nozzle over a fixed nozzle with the same exposed length can be determined.

The mass of the exit cone of the nozzle can be estimated by the following formula;⁴ a more accurate estimate can be obtained by the method of integration.

$$M = \pi \frac{\rho \bar{\delta}}{\sin \alpha} \left(\frac{d_1}{2} \right)^2 (\epsilon_{exit} - \epsilon_{entry}) + \Delta M$$

where ρ is the density of the material;
 $\bar{\delta}$ is the average wall thickness;
 α is the average exit half angle;
 d_1 is the throat diameter;
 ϵ_{exit} is the exit area ratio of the extended exit cone;
 ϵ_{entry} is the entry area ratio of the extended exit cone;
 ΔM is the mass of the deployment system;
 M is the mass of the exit cone.

Table 2 shows the estimated performance gain of the extended nozzle. Specifically, the results for three different designs of extended nozzles and for the fixed nozzle (with the same exposed length and diffusion loss) are compared. It can be seen from the table that design No. 3, which uses aluminum alloy and carbon-carbon composite material, can exceed 10s, which is 4s higher than the performance gain of the double-nested-type extended nozzle (without the gas skirt). Such a design can significantly enhance the range or the payload of the rocket.

IV. Conclusion

The development of a double-nested-type extended nozzle with a gas-deployed skirt is a very complex task; there are many issues that require further study in order to arrive at an improved and more reliable design. Clearly, by using new light-weight, high-strength metal alloys and carbon-carbon composite materials, the structural weight of this composite extended nozzle can be significantly reduced and its specific impulse can be further increased. Such a design will undoubtedly have wide range of applications on space planes and rockets.

Table 2. Estimate of the Performance Gain of Composite Type Extended Nozzles

Item name Design Nozzle type	Nozzle section								
	Nozzle performance				Exit cone		Deployed skirt		Total mass (kg)
		Throat diam. (mm)	Expansion ratio	Theoretical specific impulse	Material	Mass (kg)	Material	Mass (kg)	
Extended nozzle	1	123	45	292.1	Aluminum, silicon oxide	65.95	Niobium alloy	8.88	74.83
	2	123	45	292.1	Aluminum, silicon oxide	65.95	Niobium alloy	8.88	74.83
	3	123	45	292.1	Aluminum, carbon-carbon	50.87	Niobium alloy	8.88	59.75
Fixed nozzle	1	123	13.94	274.7	Aluminum, silicon oxide				45
	2	123	13.94	274.7	Aluminum, carbon-carbon				35

Actuator tube		Gas generator		Total system mass (kg)	Specific impulse gain (s)			
Material	Mass (kg)	Material	Mass (kg)		Increase in theoretical specific impulse	Increase in propellant	Reduction in specific impulse due to increase in structural mass	Net specific impulse gain
Steel	14.97	Aluminum, packed powder	2.14	91.94	17.4	0.534	9.95	7.98
Steel, aluminum alloy	7.92	Aluminum, packed powder	2.14	84.89	17.4	0.534	8.46	9.47
Steel, aluminum alloy	7.92	Aluminum, packed powder	2.14	69.81	17.4	0.534	7.38	10.55

References

1. Wang Chengxuan, Ma Guobao, Xiao Zhiquan, "A Survey of Foreign Development in Deployable Nozzles," FOREIGN SOLID-PROPELLANT ENGINE TECHNOLOGY, 1981 (4).
2. Wang Chengxuan, "Design and Experimental Study of Single-Section Rigid Actuator Swiveling Extended Nozzles," SOLID ROCKET PROPULSION, 1985 (3).
3. Lee Garey, John Dueringer, Geoffrey Nixon, "Convolutd Nozzle Extension," AIAA Paper No. 71~677.
4. Baker, W. H., "A Practical Guide to Extendible Exit Cone (EEC) Selection and Design," AIAA Paper No. 80~1298.

Design of Orificed Hollow Cathode for 8-cm Mercury-Ion Thruster Prototype

92FE0002A Beijing ZHONGGUO KONGJIAN KEXUE JISHU [CHINESE SPACE SCIENCE AND TECHNOLOGY] in Chinese Vol 11 No 2, Apr 91 pp 8-15

[Article by Zhang Shiliang [1728 0013 5328] and Hu Yongnian [5170 3057 1628] of the Lanzhou Institute of Physics; MS received 16 May 90]

[Text] Abstract

This paper describes the physical process of electrical discharge inside an orificed hollow cathode. Based on the design parameters of an 8-cm mercury-ion thruster and the hollow cathode, the pressure, particle density, and the energy-exchange mean free path of the initial electrons inside the cathode are calculated. From these results, the dimensions of the cathode emitter and the top orifice are determined, and the cathode emission current is estimated. The thermal equilibrium parameters and heater parameters of the cathode are calculated and compared with experimental results. The structural design of the cathode is discussed according to its operating mode in the thruster; the discussion includes selection of materials and plasma coating techniques. In addition, the results of long-term thermal-simulation experiments are also presented.

I. Introduction

In an 8-cm electron-bombardment-type mercury-ion thruster, two self-sustaining arc-discharge thermal cathodes are used. One of the cathodes whose top side is located at the center of the base plane of the ion source, is called the discharge-chamber cathode. Its main function is to initiate ion discharge and to maintain constant discharge from the chamber during normal thruster operation; the required discharge current is 0.5A. The other cathode, located outside the ion-source housing, is called the neutralizer cathode. Its function is to inject an equivalent electron current into the plasma beam in order to keep the propulsion system electrically neutral; the required discharge current is 0.55A.

In the current designs of electron-bombardment-type mercury-ion thrusters, both cathodes are orificed hollow cathodes with thermal electron emitters, as shown in Figure 1; the structures of the two cathodes are basically identical. However, since the mercury discharge through the neutralizer

cathode is one-tenth the amount of the discharge-chamber cathode, the dimensions of the top orifice and the operating parameters of the two cathodes are not the same.

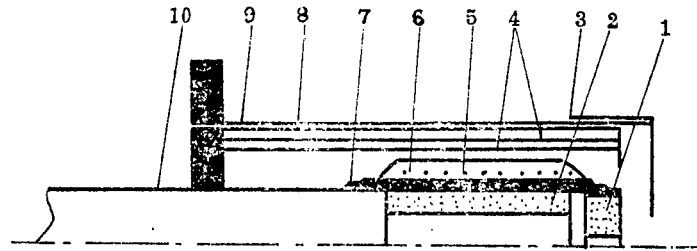


Figure 1. Structure of an Orificed Hollow Cathode

1. cathode top with center hole; 2. internal emitter; 3. contact electrode; 4. thermal screen; 5. heater; 6. Al_2O_3 coating; 7. tungsten coating; 8. tantalum sleeve; 9. ceramic tube; 10. tantalum tube

During the life of a thruster, the cathode is required to fire several thousand times; during each firing, it is subject to severe thermal shock and the bombardment of ion discharge. Therefore, the cathode is one of the components of the thruster that is the most fragile and whose performance deteriorates the fastest. For this reason, special care must be taken in selecting the cathode parameters and in its structural design. Articles on the performance, manufacturing techniques and thermal-simulation results of the discharge-chamber cathode and neutralizer cathode used in an 8-cm, 5 mN [milliNewton] mercury-ion thruster can be found in the literature; this paper will focus its discussion on the cathode design.

Because the orificed hollow cathode with internal emitter has many advantages such as low power consumption, durability and resistance against ion bombardment, it has been used successfully on the ground as a replacement for a metallic cathode in ion-coating processes and in neutral-beam injectors; the new cathode has a much longer life span and leads to improved performance of the equipment. It can also be used as an effective gas-discharge electron source in inert-gas thrusters, argon-ion lasers and high-intensity electron beams.

II. Design of the Inner Diameter of the Cathode Tube and the Diameter of the Top Orifice

In order to achieve effective ionization of the mercury atoms by the initial electrons emitted inside the cathode, and to maintain a stable discharge, it is necessary to design the cathode diameter to match the energy-exchange mean free path of the initial electrons, λ_{pr} . Thus, under a given set of conditions, the value of λ_{pr} should be first determined, and then the diameter of the cathode tube can be determined accordingly.

1. Pressure Inside the Cathode Tube

In general, different parts of the cathode tube have unequal pressures because of the motion of the mercury gas and the presence of the plasma. However, since the gas flow velocity near the small top orifice is very low, the pressure difference across the cathode primarily occurs in the immediate vicinity of the top orifice and inside the orifice channel. Therefore, one can regard the pressure to be approximately constant inside the cathode; it is referred to as the static pressure. This pressure is a function of the mercury discharge, the magnitude of the discharge current, and the diameter of the top orifice; the functional relationship can be represented by the following empirical formula:¹

$$P_0 = \frac{m}{d_0^2} (13.7 + 7.82 I_D) \times 133.3 \times 10^{-8} \quad (1)$$

where P_0 is the static pressure inside the cathode;
 m is the mercury discharge (in equivalent Amperes);
 d_0 is the diameter of the top orifice;
 I_D is the discharge current of the cathode.

2. Density of Neutral Particles Inside the Cathode

The total pressure inside the cathode is equal to the sum of partial pressures of the individual particles

$$P = n_0 k T_0 + n_e k T_e + n_i k T_i \quad (2)$$

where n and T are the density and temperature of the particles, and the subscripts 0, e, i refer to the neutral particles, electrons and ions respectively; k is Boltzman's constant.

As pointed out earlier, one can make the approximations $P = P_0$ and $T_0 = T_i = T_s$, where T_s is the cathode wall temperature. For a quasi-neutral plasma, $n_i \approx n_e$; equation (2) can then be rewritten in the following form:

$$n_0 = \frac{P_0 - n_e k (T_e + T_i)}{k T_i} \quad (3)$$

Test results show that the value of T_e remains relatively constant over a wide range of values of I_D , m and d_0 , and is equal to 0.71 ± 0.1 eV (8236K),¹ and the value of n_e is only a fraction of 1 percent of n_0 . Thus, even if $T_e = 8236K$, $T_s = 1273K$, the second term of equation (3) is only 5 percent of n_0 . As a first-order approximation, equation (3) can be written as:

$$n_0 = \frac{P_0}{k T_s} \quad (4)$$

3. Energy-Exchange Mean Free Path of the Initial Electrons

Inside the cathode, there is a high frequency of occurrence of non-elastic collisions between the initial electrons and mercury atoms and elastic collisions between the initial electrons and Maxwell electrons. The energy emitted into the plasma by the initial electrons is consumed primarily to excite and to ionize the mercury atoms; the energy exchange process involves converting kinetic energy into internal energy. The elastic collisions between the initial electrons and Maxwell electrons involve only exchange of kinetic energies, and have an effect on the energy-exchange mean free path of the initial electrons. Elastic collisions also take place between the initial electrons and mercury atoms and ions, but the frequency of occurrence is several orders of magnitude lower than that of the above-mentioned collisions; therefore, their effect can be ignored. The effective energy-exchange mean free path of the initial electrons can be expressed as:

$$\lambda_{pr} = \left(\frac{1}{\lambda_{in}} + \frac{1}{\lambda_e} \right)^{-1} \quad (5)$$

where λ_{in} is the mean free path of non-elastic collisions between the initial electrons and mercury atoms;

λ_e is the mean free path of elastic collisions between the initial electrons and Maxwell electrons.

The initial electrons emitted by the internal emitter are accelerated by the plasma sheath potential along a radial trajectory. Inside the cathode tube, they oscillate in the radial direction (because they cannot overcome the repulsive field to return to the emitter) until they collide with other particles; at the same time, they also migrate downstream under the action of the weak axial electric field, and exit the tube through the top orifice. As a result, most of the energy-exchange activities of the particles occur in the vicinity of the orifice; this is the region where plasma density is the highest, and the bombardment of ions on the emitter is the most intense, hence the temperature is also the highest. Test results show¹⁻³ that the distribution of plasma density decreases exponentially along the distance upstream from the orifice; the temperature of the emitter reaches a peak value within a narrow section at the downstream end of the tube, and decreases linearly with distance upstream. When the pressure inside the cathode exceeds 400 Pa, 90 percent of the discharge current originates from this region.

The phenomenon described above suggests that one can postulate the existence of a plasma production region where the process of electron emission and plasma production are concentrated. To simplify computation, one can also assume that the plasma parameters are uniform in this region and the position of the region is downstream of the emitter. Considering the elastic reflection of the initial electrons, the length of the plasma production region is chosen to be $L_e = 2\lambda_{pr}$. To ensure a sufficient amount of energy exchange between the initial electrons and other particles, and to maintain stable discharge inside the cathode, the emitter is designed to be a cylindrical

tube whose inner radius is equal to or greater than λ_{pr} . Thus, the length of the plasma production region and its diameter are both equal to $2\lambda_{pr}$, and the effective area of the emitter is equal to $4\pi \lambda_{pr}^2$.

By using the ion discharge model and the computer program developed by PATCRS, Wilbur et al.¹ have calculated the density of neutral particles in the plasma production region and have determined the relationship between the non-elastic collision mean free path and the density of the neutral particles, as given by the following empirical formula:

$$\lambda_{in} = \left(\frac{2.83 \times 10^{23}}{n_0} - 1.5 \right) \cdot \frac{1}{10^3 \epsilon_{pr}} \quad (6)$$

where ϵ_{pr} is the initial electron energy, which is approximately equal to the plasma potential V_p . As in the case of T_e , the value of V_p in the plasma production region does not vary a great deal over a wide range of discharge parameter values; its mean value is 8.7 eV.

The mean free path of elastic collisions between the initial electrons and Maxwell electrons is:⁴

$$\lambda_e = \frac{\epsilon_{pr}^2}{6.5 \times 10^{-17} \cdot n_e} \quad (7)$$

Substituting equations (6), (7) into (5), one obtains:

$$\lambda_{pr} = \left[\frac{6.5 \times 10^{-17} \cdot n_e}{\epsilon_{pr}^2} + \frac{10^3 n_0 \epsilon_{pr}}{2.83 \times 10^{23} - 1.5 n_0} \right]^{-1} \quad (8)$$

Once the inner radius of the emitter is known, the dimensions of the emitter can be determined, and an appropriate cathode tube (tantalum tube) which matches the emitter can be selected.

III. Estimate of the Effective Emitter Area

The analysis presented in the previous section provides a preliminary estimate of the effective emitter area. From this estimate one can determine whether the emitter surface is operating in the space charge region or the acceleration region, and whether the effective emitter area can satisfy the requirements of the 8-cm thruster (i.e., $I_D = 0.5A$).

Analysis shows¹ that the emission current is primarily produced from thermal-electron emissions; photo-induced emissions, secondary emissions and field emissions account for less than 3 percent of the total emission current.

The voltage-ampere characteristics curve of the cathode discharge shows that the cathode generally operates in a relatively flat region where the current is controlled by the contact electrode voltage;⁵ this implies that the emitter surface may operate in the acceleration region. By using the plasma

parameters given in the previous section, it is possible to estimate the surface field strength formed by the sheath layer, and to calculate its effect on the surface work function. It can be shown that the emitter surface indeed operates in the acceleration region.

The emitter surface field strength formed by the plasma sheath layer is:

$$E = \frac{dv}{dx} = \frac{V_p}{\lambda_D} = V_p \left[\frac{n_e \cdot e^2}{\epsilon_0 k T_e} \right]^{\frac{1}{2}} \quad (9)$$

where V_p is the plasma potential, chosen to be 8.7 eV;
 λ_D is the Debye length, which is of the same order of magnitude as the sheath thickness;
 e is the electron charge;
 ϵ_0 is the vacuum dielectric constant.

Because of the presence of the field strength, the value of the surface work function is reduced:

$$\phi_e = \phi_s - \left[\frac{eE}{4\pi\epsilon_0} \right]^{\frac{1}{2}} \quad (10)$$

where ϕ_e is the effective work function;
 ϕ_s is the surface work function of the material.

Also,

$$\phi_s = \phi_0 + \alpha T_s \quad (11)$$

where ϕ_0 is the work function of the material at a temperature of absolute zero; it is chosen to be 1.67 eV;
 α is the temperature coefficient of the emitter work function; it is chosen to be 2.82×10^{-4} .

If T_s is chosen to be 1273K, then from equations (11) and (10), one obtains $\phi_s = 2.03$ eV and $\phi_e = 1.83$ eV. Because of the presence of the field strength (which compresses the potential barrier), the work function is reduced by 0.2 eV. Therefore, in calculating the emitter current density, the effect of the acceleration field on the work function should be taken into account:

$$j_e = AT_s^2 \exp \left(-\frac{e\phi_e}{kT_s} \right) \quad (12)$$

where j_e is the emitter current density;
 A is the emission constant.

The discharge current passing through the top orifice consists of two parts: one is the electron current emitted by the emitter; the other is the ion

current produced by the ionization process, i.e., $I_D = I_e + I_i$. The current I_i can be calculated from the energy equilibrium relationship in the plasma production region, but is difficult to accurately compute the partial energies of the different processes taking place in the region. By incorporating the test results of the orificed hollow cathode in the calculations, it was found that when the pressure inside the cathode exceeds 400 Pa, the ratio I_i/I_D is approximately a constant (~ 0.3) over a wide range of I_D values. For the discharge-chamber cathode, $I_D = 0.5A$, hence $I_e = 0.35A$.

Substituting the values $A = 1.2 \times 10^6 \text{ A/m}^2\text{K}^2$, $T_s = 1273K$, and $\phi_e = 1.83 \text{ eV}$ into equation (12) gives $j_e = 1.14 \times 10^5 \text{ A/m}^2$. If λ_{pr} is chosen to be 0.5 mm, then the effective emitter area of the cathode is $S_K = 2\pi R \times L_e = 2\pi\lambda_{pr} \times 2\lambda_{pr} = \pi \times 10^{-6} \text{ m}^2$, $I_e = S_K \times j_e = 0.36A$, which meet the design requirements.

Based on manufacturing and assembly considerations, the following cathode dimensions are selected: emitter inner diameter 1-1.4 mm, outer diameter 2.6 mm, tube length 10 mm; it is placed in a 0.2-mm-thick tantalum tube with an outer diameter of 3 mm.

IV. Design of the Cathode Heater^{6,7}

The orificed hollow cathode is a self-sustaining arc-discharge thermal cathode. Upon ignition, the power supply to the cathode heater is immediately cut off to avoid over-heating. As the performance of the cathode emitter degrades toward the end of life, the current requirement for the emitter can no longer be met by the self-heating mode; the energy required to raise the cathode temperature must be provided by the heater. At ignition, the heater is designed to heat the emitter to a maximum temperature of 1200°C. In the heater design, precaution must be taken so that the heating filament will not evaporate due to excessive temperature, and the Al_2O_3 layer will not react with the tungsten coating or the heating filament to cause damage to the insulator or the filament.

1. Estimate of the Power Consumption of the Cathode Heater

As shown in Figure 2, the cathode heater reaches thermal equilibrium through heat dissipation in the form of radiation and conduction. The thermal equilibrium equation is:

$$P_H = P_1 + P_2 + P_3 + P_4 + P_5 + P_6 + P_7 \quad (13)$$

where P_H is the heating power of the heater;

P_1 is the radiation loss through the top of the cathode;

P_2 is the radiation loss in the radial direction through section A of Figure 2;

P_3 is the radiation loss through the annular surface downstream of the Al_2O_3 layer;

P_4 is the radiation loss through the annular surface upstream of the Al_2O_3 layer; $P_4 \approx (1/2)P_3$;

P_5 is the conduction loss through section B of the tantalum tube;

P_6 is the conduction loss through section C of the tantalum tube;
 P_7 is the amount of heat carried away by the mercury vapor as it enters the cathode and is heated from 300°C to 1200°C.

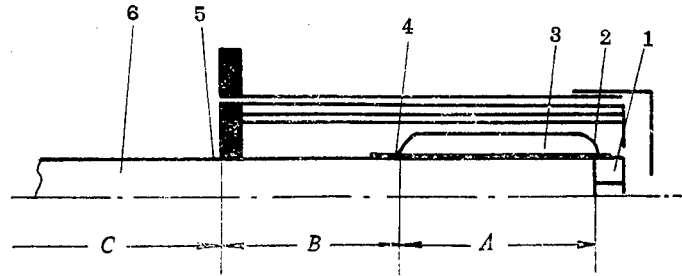


Figure 2. Temperature Distribution in the Cathode

1. cathode top, 1200°C; 2. Al_2O_3 layer, 1250°C; 3. heater, 1300°C;
 4. tantalum tube and tungsten coating, 1200°C; 5. tantalum tube, 850°C; 6. interface with mercury vaporizer, 300°C

As shown in Figure 1, the heater is buried in a layer of Al_2O_3 outside the tantalum tube; the emitter is heated to a temperature of 1200°C, and the temperature of the heating filament is approximately 1300°C. The cathode has two layers of heat screens; there is also a third screen which consists of the outer ceramic tube and the thin-wall tantalum sleeve. The temperatures shown in Figure 2 correspond to the condition when the emitter is heated to 1200°C. Except for the specified temperature value of 1200°C at the interface between section A and section B of the tantalum tube, all other temperatures are measured values. In the calculation, the temperature inside the discharge chamber of the thruster and the temperatures of those parts which are close to but not in contact with the cathode are chosen to be 80°C. The radiated power is approximated by:

$$P_r = \frac{\epsilon \sigma S_r (T - T_0)}{n + 1} \quad (14)$$

where P_r is the radiated power;

ϵ is the gray-body radiation coefficient which varies with temperature;

σ is the Stefan-Boltzman constant;

S_r is the radiation area;

T is the temperature of the radiator;

n is the number of heat screens.

The heat conduction formula is given by:

$$P_t = \frac{\lambda S_t (T_2 - T_1)}{L_t} \quad (15)$$

where P_t is the conduction loss;

λ is the conduction coefficient of the material, which varies with temperature;

S_t is the conduction cross-sectional area of the material;
 T_2 is the high temperature of the conductive material;
 T_1 is the low temperature of the conductive material;
 L_i is the length of the conductor.

In equations (14) and (15), it is assumed that the radiation surface has uniform temperature and the temperature in the conductor is linearly distributed. It is also assumed that the radiation is directed only at the vertical surface so that radiation and conduction losses can be calculated independently.

The above procedure has been used to calculate the values of $P_1 - P_6$ for emitter temperatures of 1200°C, 1100°C, 1000°C and 900°C; the results are presented in Table 1. The table also shows the measured heater power corresponding to the above temperatures.

Table 1. Estimated and Measured Heater Power of the Cathode

Power loss through different parts (W)	P_1	P_2	P_3	P_4	P_5	P_6	P_H (calculated)	P (measured)
Calculated value								
Temperature (°C)								
1200	1.1	6.17	1.5	0.8	4.0	1.6	16.5	17
1100	0.7	5.2	1.2	0.6	3.8	1.3	13.4	14
1000	0.5	4.0	0.9	0.5	3.8	0.9	11.0	11.4
900	0.4	3.0	0.7	0.4	3.4	0.6	8.9	9.2

P_7 is neglected because it is less than 0.1W. The calculated value of P_H includes a multiplier of 1.05 which accounts for hot-component/cold-end corrections. The table shows that the calculated values are basically in agreement with measured results. Among the heat-loss terms, P_2 and P_5 are the major contributors. Also, the heat filament and the insulator can operate safely even if the temperature of the emitter rises to 1300°C.

2. Heater Structure

The heater is made of 0.25-mm tungsten-rhenium wires which are wound into a 10-turn single-spiral coil with an inner diameter of 3.8 mm; it has a 15-mm lead-wire on one end. The tungsten-rhenium wire has a resistivity of 0.675 Ω -cm at 1300°C. The length of the heater is 142 mm.

The resistance of the heater is given by:

$$R = \frac{R_i \cdot L_R}{d_k^2} \quad (16)$$

where R is the heater resistance at 1300°C ;

R_1 is the resistivity of tungsten-rhenium wire at 1300°C ;

L_R is the length of the heater;

d_K is the heater diameter.

When the emitter is heated to 1200°C , the heater current is:

$$I = \sqrt{\frac{P_H}{R}} \quad (17)$$

where I is the heater current;

P_H is the heater power.

The heater uses an a.c. power supply to avoid damage to the Al_2O_3 layer by electrolysis.

V. Design of the Cathode Structure

The cathode components operate under very high temperatures; the operating condition is dictated by the operating mode of the thruster. The design of the cathode structure must take into consideration such factors as the material property under high temperature (including mercury), the structural configuration under thermal shock, the manufacturing techniques, the thermal efficiency, as well as resistance against vibration and ion bombardment for the emitter.

The emitter inside the cathode is a tubular electrode made of porous tungsten soaked into aluminate; it is produced using mature technologies and has good emission capability and high resistance against ion bombardment. One end of the emitter is welded to the tantalum filament, whose other end is welded to the inner wall of the tantalum tube.

As shown in Figure 1, the outside of the tantalum tube is coated with a layer of melted tungsten powder using plasma coating technique to prevent chemical reaction between the Al_2O_3 layer and the tantalum tube under high temperature. The Al_2O_3 is also plasma-coated to provide insulation and structural rigidity for the heater. The coating layer is rigidly attached to the base material. The coating layer has a relatively loose texture, which is designed to withstand thermal shock. In order to improve thermal efficiency, reduce cathode pre-heat time, and to avoid cracks in the coating layer due to different thermal expansion coefficients of the materials, the parts and coating layers all have very thin walls and thin layers. The tungsten-powder layer is 0.1-0.15 mm thick; the Al_2O_3 insulation layer is also 0.1-0.15 mm thick and its resistance is several megohms. The Al_2O_3 layer used to hold the heater is 0.2-0.3 mm thick. The thicknesses of the tantalum-foil heat screen, the tantalum tube, and the ceramic tube are respectively 0.01 mm, 0.2 mm, and 0.4 mm. The thin-plate cathode top with a center orifice is made of porous tungsten material; this material is chosen over dense tungsten, molybdenum or tantalum in order to keep the orifice from expansion, distortion or fusion. It is also easily welded to the tantalum tube using electron-beam welding techniques; the seam is smooth, free of cracks, and will not

deteriorate under ion bombardment. The heat filament is made of tungsten-rhenium material which has a higher re-crystallization temperature and better ductility and malleability than pure tungsten; it also has good resistance against thermal shock and vibration.

Thermal-environment simulation tests show that in the temperature range 80°C-1030°C, the cathode can withstand 13,000 thermal cycles each consisting of 4-min temperature rise and 16-min temperature drop. In the temperature range 1050°C-1100°C with no discharge, the cathode can operate for 30,000 hours without damage, and all the cathode and heater parameters remain stable. The heater resistance shows no apparent changes and the resistance of the Al₂O₃ insulation layer remains at several thousand ohms.

References

1. Siegfried, D. E., Wilbur, P. J., "A Phenomenological Model for Orificed Hollow Cathode," NASA, 1982, CR-168026.
2. Siegfried, D. E., Wilbur, P. J., "Studies on an Experimental Quartz-Tube Hollow Cathode," AIAA 79-2056, 1979.
3. Siegfried, D. E., Wilbur, P. J., "An Investigation of Mercury Hollow-Cathode Phenomena," AIAA 78-705, 1978.
4. Jahn, R. G., "Physics of Electric Propulsion," Ch. 4, New York, 1968.
5. Zhang Shiliang, Hu Yongnian, "Experimental Study of Orificed Hollow Cathode Used in Electron-Bombardment-Type Mercury-Ion Thruster," ZHENKONG KEXUE YU JISHU [VACUUM SCIENCE AND TECHNOLOGY], 1982, 12 (1), 23-31.
6. Electron Tube Design Handbook Editorial Committee, "Design of High Power Klystrons," Beijing: National Defense Industry Publishing House, 1979, 230-237.
7. Svechnikov, "Computation and Design Fundamentals of Electron Tubes," Translated by the Department of Radio of Nanjing Engineering Institute, Beijing: People's Education Publishing House, 1960, 317-327.

Theoretical Analysis of Raman Free Electron Laser Experiment Without Axial Magnetic Field

91FE0674A Beijing WULI XUEBAO [ACTA PHYSICA SINICA] in Chinese Vol 40 No 5, May 91 pp 739-747

[Article by Wang Pingshan [3769 1627 1472], Hu Kesong [5170 0344 2646], Huang Sunren [7806 1327 0088], Chen Yutao [7115 5940 3447], Fu Shuzhen [0265 3219 3791], and Hu Jianping [5170 1696 1627] of Chengdu Institute of Applied Electronics, project sponsored by the State 863 High-Technology Program: "Theoretical Analysis of Raman Free Electron Laser Experiment Without Axial Magnetic Field"; MS received 22 Jun 90]

[Text] Abstract

The self-focusing process and self-focusing ability of a double helical wiggler, commonly used in a Raman free electron laser (FEL), is analyzed. The conditions for steady beam transportation are obtained and compared to the experimental beam data from a Raman FEL without axial magnetic field. In addition, the FEL radiation data obtained on the EPA-74 electron pulse accelerator is analyzed. The theoretical analysis is in good agreement with the experimental results.

PACC: 4255T, 4060, 7845.

I. Introduction

In an FEL, the steady transport of the electron beam is influenced by the wiggler field to produce transverse oscillation. The coupling between the radiation field and wiggler field creates a ponderomotive potential which captures electrons. This leads the bunching of electrons. The kinetic energy lost by the bunched electron beam is converted into electromagnetic radiation which coherently amplifies the radiation field. Consequently, a high-power, high-efficiency coherent radiation output is produced.

FEL's may be divided into Raman and Compton FEL's. Regardless of the type, in order to understand the physics involved, it is necessary to investigate the state of electron motion and the beam transportation process. Freund¹ and Fajans² extended the work done by Friedland³ to obtain some semi-empirical results on the state of electron motion in the magnetic field of a

double helical wiggler without taking space charge into account. These results have an important impact on the understanding of the physics associated with an FEL. Furthermore, both theoretical and experimental studies show that the presence of an external guide field could enhance the power and efficiency of an FEL under certain conditions. Nevertheless, this raises issues such as difficulty of identifying the radiation mechanism.⁴ In order to overcome these difficulties, we conducted a theoretical and experimental study on the Raman FEL without an axial magnetic field. In this experiment, from a 280-A electron beam at 560 keV, the radiation output obtained has a peak power of over 7.6 MW and a frequency of 35-38 GHz.

II. Analysis of the Electronic State of Motion

Let us assume that the field experienced by an electron after an electron beam enters the homogeneous zone of the wiggler magnetic field through its adiabatic inlet is

$$\begin{aligned} \mathbf{B} &= \mathbf{B}_{ex} + \mathbf{B}_{se}, \\ \mathbf{E} &= \mathbf{E}_{ex} + \mathbf{E}_{se}, \end{aligned} \quad (1)$$

where the subscripts ex and se represent the external field and self-field, respectively. When analyzing the steady-state electron motion, the smaller radiation field is neglected. Furthermore, the higher harmonics of the wiggler field are omitted. Then, the external magnetic field may be expressed as⁵

$$\mathbf{B}_{ex} = 2B_w [I_0'(\lambda_0) \cos X_0 \mathbf{e}_{r_0} - \lambda_0^{-1} I_1(\lambda_0) \sin X_0 \mathbf{e}_{\theta_0} + I_1(\lambda_0) \sin X_0 \mathbf{e}_z] \quad (2)$$

where $X_0 = \theta_0 - k_w z$, $\lambda_0 = k_w r_0$. The static self-field of the beam is

$$\begin{aligned} \mathbf{B}_{se} &\approx -(1/2) \mu_0 n_0 e v_z r_0 \mathbf{e}_{\theta_0}, \\ \mathbf{E}_{se} &\approx -(1/2 \epsilon_0) n_0 e r_0 \mathbf{e}_{r_0}. \end{aligned} \quad (3)$$

Here, it is assumed that the beam current has axial symmetry and its density is n_0 .

Let us consider steady-state electron motion and assume that its kinetic energy remains unchanged during transportation. Then, the equation of motion is

$$d\mathbf{v}_0/dt = -e(\mathbf{E} + \mathbf{v}_0 \times \mathbf{B})/\gamma m_0. \quad (4)$$

Under the influence of the field given in equations (2) and (3), the steady-state motion of the electrons near the axis ($\lambda_0 \ll 1$, i.e., $r_0 \approx 0$) is helical with a period that corresponds to the period of the wiggler.⁵ The focusing force is from the presence of an axial gradient of the wiggler field. This effect may be recognized from the e_{r_0} component in equation (4):

$$d^2r_0/dt^2 = -eB_0(\lambda_0 v_{\theta_0} \sin X_0 + v_z \sin X_0)/\gamma m_0 + \omega_p^2 \cdot r_0/(2\gamma\gamma_z^2), \quad (5)$$

where $\omega_p^2 = n_0 e^2/(m_0 \epsilon_0)$ is the non-relativistic plasma frequency. Equation (5) also reveals that in order to have a stable transportation of the beam current, we must satisfy $\langle \sin X_0 \rangle > 0$. The symbol $\langle \rangle$ represents the average over a wiggler period. Hence, only X_0 is a constant. This means that the helical motion of the electron should be synchronous with the wiggler field. For simplicity, we substitute V_{θ_0} , the velocity without taking space-charge effect into account, into equation (5).⁵ Therefore, the conditions for stable transportation beam current are:

$$Q_0/(\beta k_{\omega} c) \leq 0.369, \quad (6)$$

$$Q_0^2 \geq \omega_p^2/(4\gamma\gamma_z^2), \quad (7)$$

where $Q_0 = eB_0/(\gamma m_0)$, $\beta = c(1 - \gamma^{-2})^{1/2}$.

However, electrons far away from the axis (not meeting the condition $\lambda_0 \ll 1$), such as the electrons on the edges of the beam used in reference 6 and in this experiment, cannot use the above approximation. In this case, a guide center approximation method^{1,2} may be used to perform the analysis.

As shown in Figure 1, electron motion is decomposed into two parts: the slow motion at the guide center and the fast motion around the center; i.e., $\mathbf{v}_0 = \mathbf{v} + \mathbf{v}_g$, $\mathbf{r}_0 = \mathbf{r}_g + \mathbf{r}$. Moreover, $|\mathbf{v}_g| \ll |\mathbf{v}|$ and $|\mathbf{r}_g| \gg |\mathbf{r}|$. Here, the subscript g represents quantities relevant to the guide center. This physical picture is basically consistent with numerical simulation.² Hence, the field exerted upon an electron can be expressed as

$$\begin{aligned} \mathbf{B}(\mathbf{r}_0) &= \mathbf{B}(\mathbf{r}_t) + (\mathbf{r} \cdot \nabla_t) \mathbf{B}(\mathbf{r}_t), \\ \mathbf{E}(\mathbf{r}_0) &= \mathbf{E}(\mathbf{r}_t) + (\mathbf{r} \cdot \nabla_t) \mathbf{E}(\mathbf{r}_t), \end{aligned} \quad (8)$$

where $\nabla_t = \partial/\partial \mathbf{r}_t$. By substituting (8) into (4) and taking the average over a wiggler period, we have

$$\begin{aligned} d\mathbf{V}_t/dt \approx & -\frac{e}{\gamma m_0} [\mathbf{E}(\mathbf{r}_t) + \langle \mathbf{V}_t \times (\mathbf{r} \cdot \nabla_t) \mathbf{B}(\mathbf{r}_t) \rangle \\ & + \langle \mathbf{V} \times (\mathbf{B}(\mathbf{r}_t) + (\mathbf{r} \cdot \nabla_t) \mathbf{B}(\mathbf{r}_t)) \rangle] \end{aligned} \quad (9)$$

$$\begin{aligned} d\mathbf{V}/dt \approx & -\frac{e}{\gamma m_0} [(\mathbf{r} \cdot \nabla_t) \mathbf{E}(\mathbf{r}_t) + \mathbf{V}_t \times (\mathbf{B}(\mathbf{r}_t) + (\mathbf{r} \cdot \nabla_t) \mathbf{B}(\mathbf{r}_t)) \\ & - \langle (\mathbf{r} \cdot \nabla_t) \mathbf{B}(\mathbf{r}_t) \rangle + \mathbf{V} \times (\mathbf{B}(\mathbf{r}_t) + (\mathbf{r} \cdot \nabla_t) \mathbf{B}(\mathbf{r}_t)) \\ & - \langle \mathbf{V} \times (\mathbf{B}(\mathbf{r}_t) + (\mathbf{r} \cdot \nabla_t) \mathbf{B}(\mathbf{r}_t)) \rangle], \end{aligned} \quad (10)$$

Here the symbol $\langle \rangle$ represents the average over a wiggler field period. The focusing process of the wiggler field may be analyzed and the state of electron motion solved based on equations (9) and (10). First, let us solve the fast component of electron motion. Equation (10) is too complicated to

solve accurately. Accurate to the first order of $\lambda(=k_w r)$, equation (10) may be written as

$$dv/dt \approx \omega_p^2 r / (2\gamma r_z^2) \mathbf{e}_r - e \mathbf{V} \times (\mathbf{B}(\mathbf{r}_z) + (\mathbf{r} \cdot \nabla_z) \mathbf{B}(\mathbf{r}_z)) / (\gamma m_0). \quad (11)$$

In order to analyze the steady-state motion of the beam and its focusing process, it is necessary to analyze the component \mathbf{e}_r of equation (11):

$$\begin{aligned} \ddot{r} - (V_\theta)^2/r &= \omega_p^2 r / (2\gamma r_z^2) \mathbf{e}_r - (2B_\omega e / \gamma m_0) \cdot [V_\theta I_1(\lambda_z) \sin X_z \\ &\quad + V_z I_1(\lambda_z) \sin X / \lambda_z + V_z I_2(\lambda_z) \cos X_z \sin(\theta - \theta_z) \\ &\quad + (V_\theta I_1(\lambda_z) r / r_z) \sin X + I_2(\lambda_z) k_\omega V_\theta \cos(\theta - \theta_z) \sin X_z \\ &\quad + (V_z I_2(\lambda_z) / r_z) \sin(X + \theta - \theta_z)]. \end{aligned} \quad (12)$$

According to our assumption, $\langle \sin X_g \rangle \approx 0$, $\langle \sin(\theta - \theta_g) \rangle \approx 0$, $\langle \cos(\theta - \theta_g) \rangle \approx 0$, and $\langle \sin(X + \theta - \theta_g) \rangle \approx 0$ in the electron motion. Hence, these corresponding terms do not have any focusing effect. Only when $\langle \sin X \rangle > 0$ does the gradient of the axial component of the wiggler field have a constraining effect on the fast motion of the electrons. In this case, X is a constant. In order to find a specific solution of this fast motion component, as an approximation (as well as for simplicity), the space-charge effect of the beam current and the gradient component of the field are not considered. Hence,

$$d\mathbf{V}/dt \approx -e(\mathbf{V} \times \mathbf{B}(\mathbf{r}_z)) / \gamma m_0. \quad (13)$$

Let us choose the following helical coordinates: $\mathbf{e}_1 = \mathbf{e}_r \cos X - \mathbf{e}_\theta \sin X$, $\mathbf{e}_2 = \mathbf{e}_r \sin X + \mathbf{e}_\theta \cos X$, $\mathbf{e}_3 = \mathbf{e}_z$. Then, the steady-state motion of the electrons with a period $k_w z$ can be solved as follows:

$$\mathbf{V} = V_z \mathbf{e}_z + V_\omega \mathbf{e}_1, \quad (14)$$

where $V_\omega = \Omega_\omega I_0(\lambda_g) / k_\omega$, $\Omega_\omega = e B_\omega / \gamma m_0$, and $X = \pi/2$. Therefore, the major fast motion component is a helical motion around the guide center.

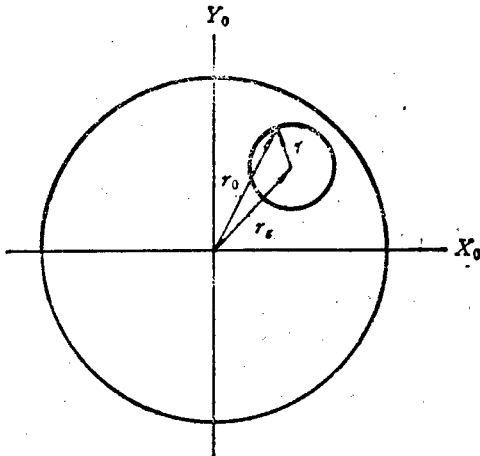


Figure 1. Beam-Current Cross Section and Selection of Coordinate System

Nevertheless, equation (14) does not take into account the effect of limited helical radius on the motion. When the wiggler field is relatively strong, this effect cannot be neglected. A semi-empirical expression which takes into consideration the limited helical radius is introduced in the analysis.

$$V_w = 2Q_w V_z I_0(\lambda_z) I_1(\lambda) / (\lambda(k_w V_z - 2Q_w I_0(\lambda_z) I_1(\lambda))). \quad (15)$$

Substituting V_0 into (12), one gets the stability conditions for fast electron motion as follows:

$$(Q_w I_0(\lambda_z))^2 \geq \omega_p^2 / (4\gamma\gamma_z^2), \quad (16)$$

$$Q_w I_0(\lambda_z) / \beta k_w c \leq 0.369. \quad (17)$$

Substituting (15) into (9), it is possible to obtain the equation of motion for the guide center.

$$d\mathbf{V}_g/dt \approx \omega_z \mathbf{e}_z \times \mathbf{V}_g + \Delta\omega/2r_z - V_{gz} \omega_p^2 \beta_z r_z / \gamma c \mathbf{e}_z, \quad (18)$$

where $\omega_z = -Q_w V_w / V_z$, $\Delta\omega = -Q_w k_w V_w + \omega_p^2 / 2\gamma\gamma_z^2$.

The transverse component may be written as

$$(d^2/dt^2 + Q_1^2)(d^2/dt^2 + Q_2^2) \begin{pmatrix} X_g \\ Y_g \end{pmatrix} = 0, \quad (19)$$

where $Q_{1,2}^2 = (\omega_z^2 - \Delta\omega)/2 \pm \omega_z(\omega_z^2 - 2\Delta\omega)^{1/2}/2$.

When the wiggler field amplitude is small, we get

$$Q_{1,2}^2 = (Q_w^2 - \omega_p^2 / \gamma\gamma_z^2) / 2. \quad (20)$$

Hence, equation (19) becomes

$$(d^2/dt^2 + Q^2) \begin{pmatrix} X_g \\ Y_g \end{pmatrix} = 0. \quad (21)$$

The solution to equation (21) is the transverse motion of the electron guide center, i.e., Betatron motion. In order to have stable electron motion, in addition to having a steady fast helical motion, its Betatron motion must also be stable, i.e.,

$$Q^2 \geq \omega_p^2 / \gamma\gamma_z^2. \quad (22)$$

The beam-expanding effect from the space charge is offset by the presence of an axial component of the wiggler field (when $\lambda_g \leq 1$, this component is proportional to r_g).

In summary, the transverse inhomogeneity of the double helical wiggler can confine the electron beam. However, the beam-confining process is far more complicated than that described in reference 7. In order to achieve steady beam current transportation, the relevant parameters must satisfy equations (17) and (22).

In addition, it is revealed in reference 2 that when space charge is not considered and if the axial magnetic field is small or absent, there is a substantial difference between the numerical simulation and the approximation results at the center due to faster Betatron motion. However, the analysis shown above shows that Betatron motion can be slowed down by space-charge effect and the Raman FEL theory can still be applied when there is no axial magnetic field.

III. Theoretical Considerations of Raman FEL Without Axial Magnetic Field

The basic physical process in a Raman FEL can be viewed as an energy transfer process involving the coupling of the waveguided electromagnetic wave and the space charge wave to amplify the electromagnetic wave⁸ in an applied wiggler field. The dispersion relations are:

$$\omega^2 = c^2 k^2 + \omega_c^2, \quad (23)$$

$$\omega = (k + k_w)\beta_z c + p_1 \omega_p / \gamma_z \gamma^{1/2}, \quad (24)$$

where $\omega_c^2 = \omega_{c0}^2 + p_2 \omega_p^2 / \gamma$ is the effective cutoff frequency of the waveguide, ω_{c0} is the cutoff frequency of the waveguide in vacuum and p_2 can be treated as a filling factor for the energy of the electromagnetic wave in approximation. The energy transfer primarily takes place at the frequency synchronous to the slow space-charge wave, i.e.,

$$\omega = \beta_z c k_{\omega_c} \gamma_z^2 \{1 \pm \beta_z (1 - (\omega_c / (k_{\omega_c} \gamma_z \beta_z c))^2)^{1/2}\}, \quad (25)$$

where $k_{\omega_c} = k_{\omega} - p_1 \omega_p / (\gamma_z \gamma^{1/2} \beta_z c)$ is the effective wave number of the wiggler field. Theoretical analysis⁹ and experimental results¹⁰ indicate that the low-frequency radiation gain is low for equation (25). Furthermore, it is not of concern to this work, and therefore will not be taken into consideration.

The Raman FEL gain is the ratio of the radiation power at z to that at l ($<z>$)¹¹ (relative to the amplifier $l = 0$):

$$G = p(z)/p(l) = |a(z)/a(l)|^2, \quad (26)$$

where $|a(z)/a(l)|$ is the ratio of the electric field amplitudes, which can be expressed as

$$a(z)/a(l) = \sum_i A_i \exp(jk_i(z-l)), \quad (27)$$

The summation is with respect to all mutually interactive radiation fields, A_i is the normalized amplitude of a radiation field, and k_i is its complex propagation constant. They can be derived from the poles and remainders in dispersion equations:¹²

$$A(\delta k) = D/F, \quad (28)$$

where $D = (\delta k - \theta + \theta_p + i\theta_i)(\delta k - \theta - \theta_p + i\theta_i)$, $F = \delta k(\delta k - \theta + \theta_p + i\theta_i) \cdot (\delta k - \theta - \theta_p + i\theta_i) + Q$, $\theta = (\omega/\beta_z c) - k - k_\omega$ is an "out-of-tune factor" of the FEL, $Q = p_2 \beta_z^2 k_\omega^2 \gamma_z^2 \theta_p^2 (1 + \beta_z)^2 / (4k p_i)$ represents the intensity of energy exchange between the two waves, $\theta_p = p_1 \omega_p / (\gamma_z \gamma^{1/2} \beta_z c)$ is the normalized plasma frequency, $\theta_i = \sqrt{8\pi} \omega \Delta \gamma_z \exp(-2Q^2/\Delta) (Q/\Delta)^4 / (\gamma_z^2 \beta_z^2 c)$ is the normalized Landau damping rate. Here, $Q = p_1 \omega_p \gamma_z / (\omega \gamma^{1/2})$, $\Delta = \Delta \gamma_z / (\gamma_z^2 \beta_z^2)$. Therefore, for a "cold" electron beam, $\Delta \gamma_z / \gamma_z \rightarrow 0$, $\theta_i \rightarrow 0$. Or, $\Delta \gamma_z / \gamma_z \approx 3\%$ is a constant; when the beam current increases to a certain value, $\theta_t \rightarrow 0$. This indicates that Landau damping is very small and can be neglected. In our experimental system, $\Delta \gamma_z / \gamma_z \approx 3\%$. As long as $I_T \geq 40A$, the effect of Landau damping can be neglected and the beam can be considered as a cold beam. Thus, equation (28) can be written as:

$$A(\delta k) = (\delta k - \theta + \theta_p)(\delta k - \theta - \theta_p) / (\delta k(\delta k - \theta + \theta_p)(\delta k - \theta - \theta_p) + Q). \quad (29)$$

When $\theta = -\theta_p$ (which corresponds to the situation of (25)), the maximum gain rate ($\tau = \text{Im}k$) of the Raman FEL is

$$|\tau| = \beta_z k_\omega (1 + \beta_z) \gamma_z^2 (p_2 \omega_p)^{1/2} / (2 \sqrt{2} (p_1 \gamma_z \gamma^{1/2} \beta_z c)^{1/2}). \quad (30)$$

This is the space gain rate in the linear gain region. When most electrons are captured by the ponderomotive force and transfer some energy to the radiation field, the radiation output saturates. This corresponds to the situation in our experiment when the mutual interaction zone was approximately 1 m long. The maximum radiation output efficiency is determined by that state. However, in principle, linear theory should not be applied to theoretically analyze FEL efficiency. Instead, a nonlinear theory that describes the saturated state should be employed. Nevertheless, theoretical analysis shows that linear theory may be used to estimate FEL efficiency.¹¹ Furthermore, for an FEL with a magnetic wiggler, the estimated value based on linear theory is in good agreement with the result from self-consistent nonlinear theory.¹³ The saturation efficiency of FEL is:¹¹

$$\eta = (\beta_z / \beta)^{1/2} \gamma_z (1 + \gamma) \lambda p_1 \omega_p / (c \pi \gamma^{3/2}). \quad (31)$$

IV. Comparison of Experimental Results to Theoretical Analysis

The Raman FEL experimental system without an axial magnetic field is shown in Figure 2. This system was successfully used to carry out spontaneous radiation amplifier Raman FEL experiments.

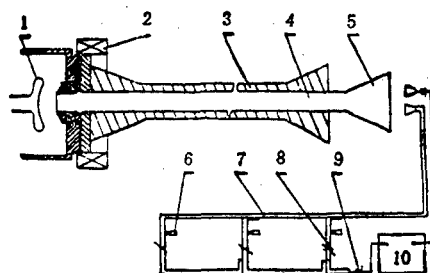


Figure 2. The EPA-74 Raman FEL System Without an Axial Magnetic Field

1. cathode; 2. lens; 3. wiggler; 4. drift tube; 5. output horn; 6. attenuator; 7. dispersion line; 8. band-pass filter; 9. crystal rectifier; 10. oscilloscope

An electron beam, 560 keV in energy, 100-300 A in intensity, 3 percent in energy dispersion, $0.06 \text{ cm-rad}(\epsilon_N)$ in emissivity, and approximately 1 cm in diameter, enters the 1.7-m-long drift tube which is pumped to vacuum. The diameter of the tube is 1.6 cm. A circularly polarized wiggler field, 3.45 cm per period, is generated by a 1.5-m-long concentric double helix mounted on a nylon rack. A 7-cycle adiabatic input segment guarantees the adiabatic transition of the beam to the homogeneous zone of the wiggler field. It has a helical trajectory such as that described in section II of this paper. When the wiggler field was measured to be 1.25 kGs by using an 8-mm dispersion line measuring system¹⁴ and a microwave calorimeter, the radiation frequency is 35-38 GHz, energy is 41-48 mJ, and peak power is 7.6 MW. The following is an analysis of the experimental data based on the results described in sections II and III.

1. Beam Current Transportation

Figure 3 shows the beam current transportation results without an axial magnetic field. It shows that, within a certain range, the transported beam current increases with rising wiggler field. However, when the wiggler field amplitude is too large, beam current drops. A similar result was obtained at the Naval Research Laboratory.¹⁵ This result was analyzed using equations (17) and (22). From (17), in order to maintain the desired helical motion, the wiggler field must not be too high. For our experimental system, it should be $B_w < 1700 \text{ Gs}$. When the wiggler field reaches a certain value (or the beam diameter is enlarged due to emissivity or space-charge effect and the magnetic field at the edge of the beam is increased to a certain value), equation (17) is no longer satisfied and the electron beam suffers some loss. Hence, in Figure 3(a) when the wiggler field reaches a certain level, the beam current declines with increasing magnetic field. With increasing transportation distance, the beam current also falls due to losses, as shown in Figure 3(b). Curve 3 in Figure 3(b) was obtained after the coaxial system was fine-tuned. Therefore, the induced current and transported current are larger than those in curves 1 and 2.

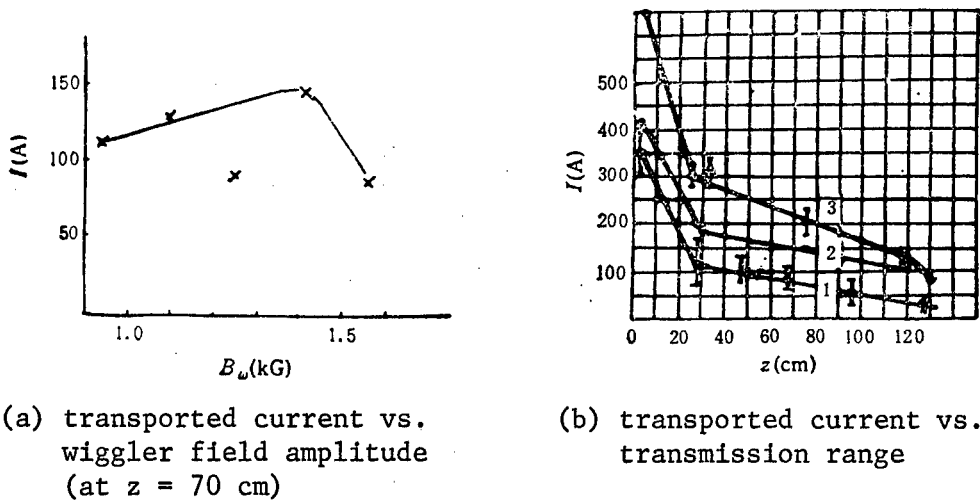


Figure 3

In order to have stable transportation of beam current, the Betatron motion must also be stable. Equations (17) and (22) can be used to obtain the threshold stable beam current as shown in Figure 4. One can see that the stronger the wiggler field is, the higher is the current that is allowed to maintain a stable beam motion. This is consistent with the pattern observed in the experiments. The numerical difference is caused by these facts: 1) a large number of electrons are lost in the adiabatic transition segment of the wiggler field (electrons that passed the segment should obey the pattern shown in Figure 4 even in the absence of other fields) and the beam current at the start of the homogeneous zone of the wiggler field is smaller; 2) the injected beam is not an ideal parallel beam, which leads to divergence and losses; and 3) equation (22) is derived under certain ideal conditions. This is somewhat different from reality, especially when the wiggler field amplitude is too strong. However, the above analysis shows that as long as we can deliver a high-quality electron beam below the threshold to the homogeneous zone of the wiggler field, the wiggler field is capable of confining the beam. Moreover, this confining force is very strong. Kirkpatrick⁶ used a double helix wiggler field with a 3.14-cm period to confine and transport a 2.2-MeV, 930-A electron beam across the wiggler field of 1.3-1.5 kGs.

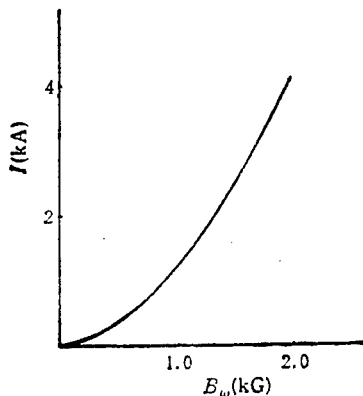


Figure 4. Beam Current Confining Threshold, $\gamma = 2.067$, $\lambda_w = 3.45$ cm

Curves 1, 2 and 3 correspond to experiments 1, 2 and 3. Distance z starts from the entrance of the wiggler. $B_w = 1.25$ kG for curves 1 and 3 and $B_w = 1.44$ kG for curve 2.

2. Analysis of Radiation Output

In these experiments, because the beam radius is relatively large, the three-dimensional theory described in sections II and III is used. Equations (15) and (25) can be used to determine the radiation frequency and mode of the Raman FEL as a function of other parameters, as shown in Figure 5. At $\lambda_\omega = 3.45$ cm and a beam energy of 560 keV, in our experimental system only the TE_{11} and TM_{01} modes may exist. There are two reasons why it is hard to operate in mode TM_{01} : 1) In the experiment, in order to ensure good beam transportation to conduct an effective Raman FEL experiment, B_ω is chosen to be between 1 and 1.5 kGs. This kind of magnetic field falls outside mode TM_{01} . 2) It is difficult for an electron beam injected concentrically with respect to the drift tube with current concentrated near the axis to excite mode TM_{01} , whose transverse electric field component on the axis is zero. Figure 6 shows typical beam current, beam voltage and radiation output waveforms. The narrowing of the radiation output pulse might be caused by the narrowing or variation of the beam current and energy.

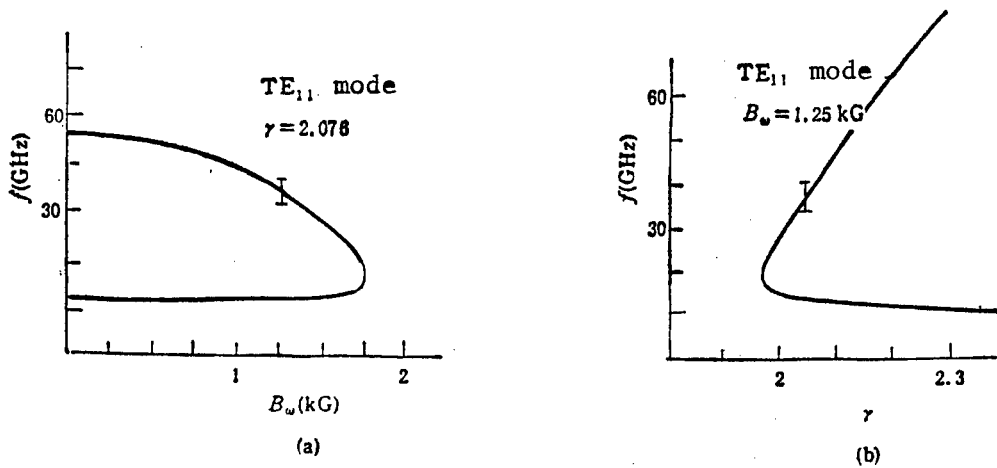


Figure 5. Radiation Output Frequency vs. (a) Wiggler Field
(b) Electron-Beam Energy. I is the experimental value.

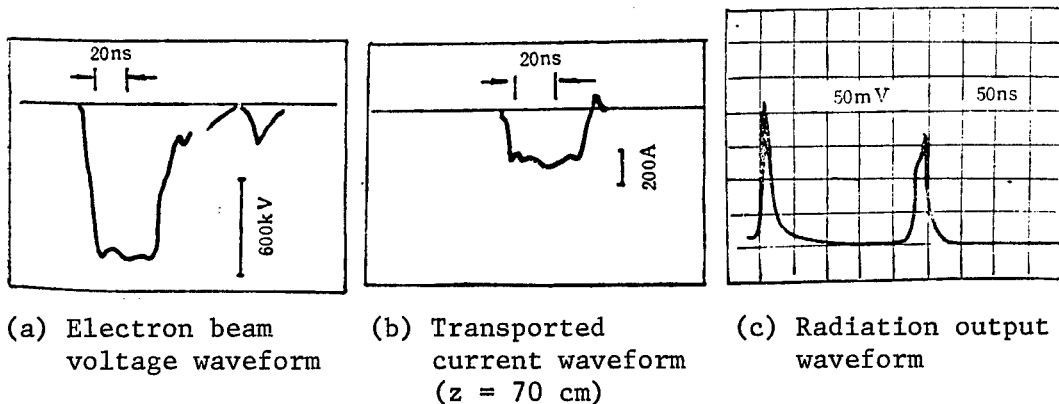


Figure 6. Typical Signal Waveforms

Under the conditions that B_w is 1.25 kGs, beam current is 280 A, beam energy is 560 keV, and beam diameter is 1 cm, the measured FEL gain curve is as shown in Figure 7. Under these conditions, $p_1 \approx 0.85$ and $p_2 \approx 0.6$. Figure 7(b) shows the spatial radiation growth rate curve derived from equation (30). It is in excellent agreement with measured results.

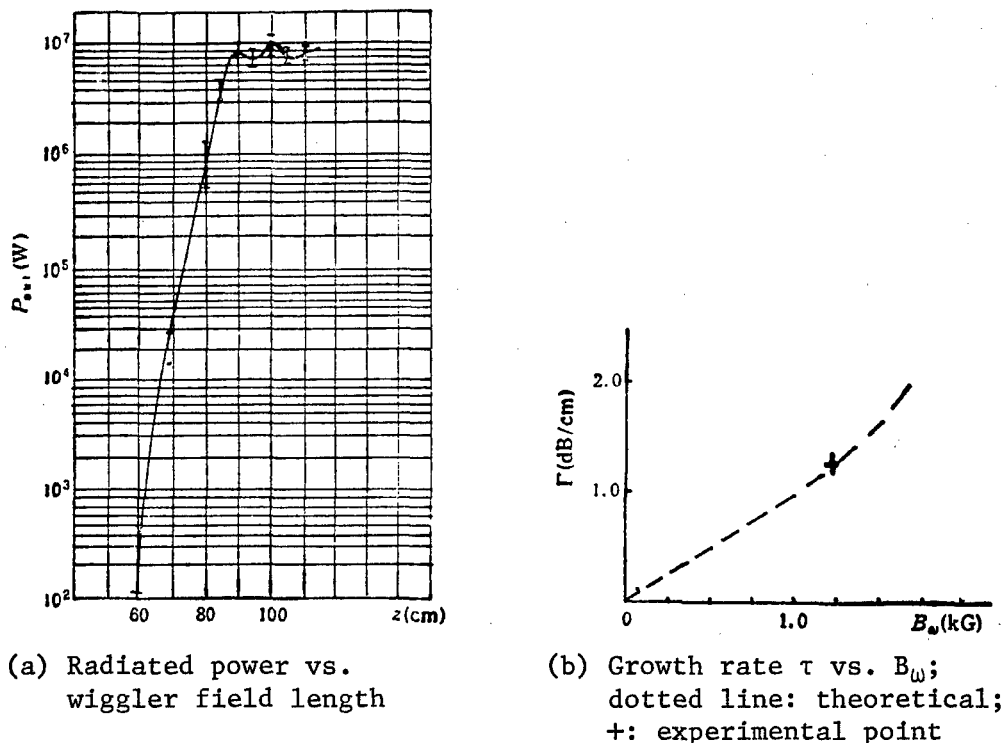


Figure 7

After passing through the linear gain region, radiation saturates at approximately 1 m in the mutual interaction zone. The saturated power is 7.6 MW, which corresponds to a 5 percent efficiency. This is quite different from the theoretical 10 percent efficiency, probably because of beam quality and precision of the wiggler field.

V. Conclusions

From the above, we can conclude that:

(1) Due to inhomogeneous spatial field distribution, electrons away from the axis, in addition to the fast helical motion around the guide center at a period of $k_w V_z$, also have a relatively slow motion with respect to the guide center. The space-charge effect further slows down this motion. Consequently, within a certain range, the electron motion without an axial magnetic field can still be adequately described by the guide center approximation in the analysis of the physical processes of a Raman FEL.

(2) Experimental results obtained with the EPA-74 Raman FEL agree well with the theoretical analysis.

References

1. H. P. Freund, et al., IEEE J. QUANTUM ELECTRONICS, QE-21 (1985), 1073.
2. J. Fajans, et al., PHYS. REV., A32 (1985), 3448.
3. L. Friedland, PHYS. FLUIDS, 23 (1980), 2376.
4. G. Bekefi, et al., PHYS. FLUIDS, 28 (1985), 3177.
5. P. Diament, PHYS. REV., A28 (1981), 1436.
6. D. A. Kirkpatrick, et al., PFC/JA-88-26.
7. Ping King Tien, J. APPL. PHYS., 25 (10) (1954), 1282.
8. P. Sprangle, et al., in "Infrared and Millimeter Waves," edited by K. J. Button, Academic, New York, (1978), Vol 1, p 279.
9. H. P. Freund, et al., PHYS. REV., A28 (1983), 3438.
10. J. A. Pasour, et al., PHYS. REV. LETT., 53 (1984), 1728.
11. A. Gover, et al., IEEE J. QUANTUM ELECTRONICS, QE-17 (1981), 1196; also E. Jerby, et al., IEEE J. QUANTUM ELECTRONICS, QE-21 (1985), 1041.
12. J. Fajans, et al., PHYS. FLUIDS, 29 (10) (1986), 3461.
13. P. Sprangle, et al., PHYS. OF QUANTUM ELECTRONICS, 7 (1980), 207.
14. Chen Yutao, et al., QIANG JIGUANG YU LIZI SHU [HIGH-POWER LASER AND PARTICLE BEAMS], 1 (1), 1989, p 40.
15. J. A. Pasour, et al., IEEE J. QUANTUM ELECTRONICS, QE-21 (1985), 845.

Performances and Possible Uses of Far Infrared Free Electron Lasers

40100001A Shanghai GUANGXUE XUEBAO [ACTA OPTICA SINICA] in English Vol 11
No 8, Aug 91 pp 708-713

[Article by R. Coisson, Department of Physics, University of Parma, Italy,
and Fu Ensheng, Shanghai Institute of Optics and Fine Mechanics, Academia
Sinica, Shanghai, China; MS received 7 Nov 90, revised 11 Feb 91]

[Text] Abstract

In this paper the advantages of the realisation of a far infrared (FIR) free electron laser (FEL) are shown: it requires an electron beam with less stringent characteristics, less expensive and it is unique source for non-linearity and coherence in FIR. The dependence of the FEL performance on parameters of the electron beam and undulator is described. For a given beam emittance there is a specific wavelength below which the gain rapidly becomes very low. The important physical phenomena in the FIR and possible uses of FIR FEL are given in broad outline, these studies could be important for the possible development of a THz electronics.

Key words: Far infrared; Free electron laser.

I. Introduction

The free electron laser (FEL), based on stimulated emission of radiation from ultrarelativistic electron beams in an undulator (periodic transverse magnetic field) has caused great interest for its possibilities to extend the range of electron beam devices (travelling wave tubes etc.) to shorter wavelengths than the microwaves (cm-waves) used up to now. Since the first operation of a FEL oscillator in 1976, although slowly (as their construction is not easy), a number of FEL oscillators have been operated, in the range from mm-waves to the visible range. Some of them are beginning or will soon be used as user facilities.¹⁻⁴ Efforts are under way to extend the range of FELs as far as possible into the VUV; however their possible actual use is not in the near future.

The far infrared (FIR) region of the spectrum is the range extending approximately from 40 μm to 1 mm wavelength.

In this paper we want to show the advantages of the realisation of a far infrared (FIR) FEL particularly for three reasons:

- 1) The operation at longer wavelengths is less delicate and requires an electron beam with less stringent characteristics.
- 2) As it requires a lower energy machine, a FIR FEL is less expensive than in the near IR.
- 3) There is a lot of interesting physics to do in the FIR with an intense, short pulse and tunable source, and the FEL is the only source having all these characteristics in the FIR.

First we describe the dependence of the FEL performance on its parameters, and then we indicate some of the fields of application in the FIR.

II. FEL Characteristics

Let γmc^2 be the electron energy ($\gamma \gg 1$) and \hat{I} the peak current, λ_0 the undulator period, and $K = eB_0\lambda_0/2\pi mc$ its "deflection parameter". The range of operating wavelengths is defined by^{5,6}

$$\lambda = \frac{\lambda_0}{2\gamma^2} (1 + K^2/2). \quad (1)$$

The efficiency can be of the order of $1/2 N$ (N = number of period), but even higher with a tapered undulator. The peak power is then $P_L \approx \gamma mc^2 \hat{I} / 2N$.

The important parameter determining how easily oscillation can be obtained is gain. The dependence of gain on wavelength is of course depending on which parameters we keep constant.

A condition that practically has to be satisfied to have a useful gain is that the electron beam is matched to the (diffraction-limited) mode of the emitted radiation in the cavity. That means that the electron beam transverse sizes are

$$\sigma_x \approx \sigma_y \approx (L\lambda/2\pi)^{1/2}, \quad (2)$$

($L = N\lambda_0$ length of the undulator) and the divergences

$$\sigma_x' \approx \sigma_y' \approx (\lambda/L)^{1/2}. \quad (3)$$

In accelerator terms, this means emittance

$$\varepsilon \approx \lambda/2\pi, \quad (4)$$

and full coupling (equal vertical and horizontal emittances), and beta function of the order of $L/2\pi$. A smaller emittance would give the same gain, but it would be more difficult to get the same current.

Another necessary condition is that the electron energy spread should be small:

$$\Delta\gamma/\gamma \leq 1/2 N. \quad (5)$$

The gain is also reduced if the electron bunch is shorter than $N\lambda$: so we should have

$$\Delta t \geq N\lambda/c, \quad (6)$$

Δt is the slipping time of one optical wavelength for each wiggler period, then it might be useful to use a "debuncher" (or "energy compressor") where $\Delta\gamma$ is decreased while Δt is increased.⁷

In case, changing wavelength, we change the beam size and divergence in order to always satisfy the previous conditions, the gain can be expressed in the form

$$g \simeq 5.9 \frac{\hat{I}}{I_A} N^2/\gamma, \quad (7)$$

where $I_A \simeq 17045$ A is the Alfvén current, \hat{I} is the peak current.

More conservatively, taking into account that when in eqs. 4, 5 equalities hold, there is a gain reduction of a factor ~ 2 , we could put 1 instead of 5.9 in eq. 7.

If the gain is high,^{8,9,6} the single-pass gain increases exponentially:

$$g_h \simeq \frac{1}{g} \exp(2.7 g^{1/3}), \quad (8)$$

and there is the large accompanying optical phase shift.

But eqs. 7-8 are applicable only in the conditions (4, 5), while when some value exceeds these, the gain decreases very rapidly. Then for a given beam emittance there is a wavelength below which the gain rapidly becomes very low.

From the point of view of designing a machine for a given output wavelength, its emittance can grow in proportion to λ . If the obtainable current can be estimated to be proportional (for a given duty cycle and bunch length) to

$$\hat{I} \simeq B_e \gamma^2 \epsilon_x \epsilon_y, \quad (9)$$

with B_e depends on the electron gun and is of the order of 10^8 - 10^{10} A/m² (possibly up to 10^{12}).

In practice then eq. 7 can be written as:

$$g = AN^2 \gamma \lambda^2 = AN^2 \lambda_0^{1/2} \lambda^{3/2}, \quad (10)$$

where $A \approx 150 \text{ m}^{-2}$ for $B_e \approx 10^8 \text{ A/m}^2$ if we use the factor 1 (instead of 5.9) in eq. 7.

We see that even in the range of wavelength longer than the minimum defined by the beam emittance, the gain tends to increase considerably with wavelength.

Also, the lower value of γ necessary to reach a longer λ make the machine less expensive.¹⁰

A table of examples, for an undulator with $\lambda_0 = 5 \text{ cm}$, $N = 75$, $K = 1$ and an electron gun with $B_e \sim 10^8 \text{ A/m}^2$:

γ	60	40	20
$I \text{ (A)}$	1	2.2	9
$\lambda \text{ (}\mu\text{m)}$	10.4	23.4	94
g	0.5%	2%	15%

The effect of energy spread does not depend on wavelength (see eq. 5): but the availability of a higher gain allows to use a lower value of N , a better tolerance to $\Delta\gamma/\gamma$ can be obtained, at the expense of a decrease in gain by a factor N^2 : but the decrease in gain due to energy spread is exponential, so an optimum is found for a value comparable with the condition (5), with a peak current proportional to $1/N$. An "energy compression" could be good both for satisfying eq. 5 and eq. 6 (at the expense of a reduction in peak current).

The temporal structure of the light pulse (as long as the beam length is $> N\lambda$) is equal to that of the electrons, e.g., in linacs this is a few picoseconds.¹¹

The linewidth is close to the Fourier transform limit:

$$\Delta\omega/\omega \simeq \lambda/2\sigma, \quad (11)$$

III. Other FIR Sources

1) Up to now, most of the work on FIR has been done with "blackbody" sources with Fourier-transform spectroscopic detection (with a Michelson interferometer). These are very weak incoherent sources and their use is limited to absorption spectroscopy.

2) Information on this spectral region can be obtained by Raman spectroscopy in the visible range. The physical information obtained is often complementary to the previous measurements, as there are different selection rules.

3) Several laser sources have been developed in the FIR: methanal, formic acid, etc., pumped by CO_2 lasers. These are coherent continuous-wave sources of many mW,¹³ and some studies of coherent radiation-matter interactions have been done with them.¹⁴ However, although there are many lines, they are almost not tunable.

4) A widely tunable continuous-wave FIR source can be obtained by mixing two singlemode CO₂ lasers on a point-contact diode.¹⁵ However, the power is in the nano watt (nW) range, and it is not suitable, e.g. for nonlinear spectroscopy.

*In conclusion we see that the FEL offers the possibility of a source with wide continuous tunability, high peak power, short Fourier-transform-limited pulses, that are superior to all other sources.

IV. Physical Phenomena in the FIR

The range of phenomena of interest in connection with the FIR spectrum is very wide. For example:¹⁶

--Superconductor gaps have energies corresponding to the FIR.

--"Hot" electrons in GaAs/GaAlAs junctions, sub-bands in GaAs/GaAlAs superlattices and quantum wells are phenomena showing FIR resonances and fast decays to be studied with short pulses, and their coherent and nonlinear behaviour is of interest in connection with possible electronic devices.

--Plasmons in semiconductors can have all resonance frequencies from the visible to the FIR.

--Low-energy electronic excitations of impurities in crystal lattice show narrow atomlike lines.

--Molecular gas rotations.¹⁷

--Intermolecular vibrations in molecular crystals.

--Antiferromagnetic resonances are often in the sub-mm range.

V. Possible Uses of FIR FEL

Essentially, the whole FIR spectrum can be covered by blackbody sources or CO₂-point contact diode mixers. But there are essentially two aspects that are not studied by these sources, and only in a limited way by FIR gas lasers:

--High (instantaneous) intensities (which need high brightness) of FEL allows excitation of physical systems in the nonlinear regime.

--High intensity coherent (Glauber-state) short pulses allow coherent excitation of physical systems, that is to study phenomena that can not be described by "rate equations" alone, or, in terms used in microwave magnetic resonance, to measure the T₂ (dephasing time) as well as the T₁ (energy decay time).

Then, in thinking about the use of FIR FEL, one should not only think to the materials that have FIR resonances, but to the aspects for which the FEL is unique; nonlinearity and coherence.

It is probably only with the FEL that materials can be studied for their possible use as solid-state FIR sources, mixers, modulators etc., and this might open the possibility of extending the microwave electronics to frequencies of the order of a terahertz ($1 \text{ THz} = 10^{12} \text{ Hz}$).

In the last two years, some experiments have been done with the Santa Barbara 100-400 μm FEL.¹

VI. Example: the Hefei (USTC) Linac FEL

At the USTC in Hefei (Anhui), an experiment is under way to study a linac-based FEL at 10 μm wavelength.¹⁸ At present the linac beam characteristics have still to be improved in order to obtain enough gain for oscillation at 10 μm .

It is interesting to see how operation at 100 μm would give a higher gain and could be obtained with a lower beam quality. The present characteristics are: $\gamma = 40-80$, $\epsilon = 5\pi \cdot 10^{-6} \text{ m. rad}$, $\Delta\gamma/\gamma \approx 10^{-2}$.

With an undulator of 98 periods of 3 cm and $K = 0.8$, the output at $\gamma = 44$ is $\lambda = 10 \mu\text{m}$.

The gain is very low because eq. 4 is not satisfied (and some reduction comes also from eq. 5).

At 100 μm eq. 4 would be satisfied, and the gain, with $\gamma = 15$, would be more than 20 percent, which is comfortable. The same could be obtained at $\gamma = 30$ with an undulator with $N = 75$ and $\lambda_0 = 10 \text{ cm}$.

VII. Conclusions

It seems not only realistic and less expensive to aim first at realising a FEL in the FIR (before aiming at near IR or UV), but also there is a particular interest in the fact that many nonlinear and coherent phenomena in the FIR can be studied almost only with the FEL (while, e.g. in the near IR and visible there are high peak power, tunable lasers, continuous-wave or short pulse (Fourier-transform limited), as well as mirrors, modulators, fibres,...), and these studies could be important for the possible development of a THz electronics.

References

1. L. R. Elias, V. Jaccarino, W. M. Yen, NUCL. INSTRUM. & METH., 1985, A239, No 3 (Sep), 439-442.
2. G. S. Edwards, N. H. Tolk, NUCL. INSTRUM. & METH., 1988, A272, Nos 1/2 (Oct), 37-39.
3. P. W. Van Amersfoort, et al., NUCL. INSTRUM. & METH., 1989, A285, Nos 1/2/3, 67-70.

4. J. M. Ortega, et al., NUCL. INSTRUM. & METH., 1989, A285, Nos 1/2/3, 97-103.
5. G. Dattoli, A. Renieri, "Laser Handbook," Vol 4, Ed. M. L. Stitch and M. Bass (North Holland, Amsterdam 1985).
6. See the proceedings of any recent FEL conference, for ex. in NUCL. INSTRUM. & METH., 1985, A239, No 3; 1988, A272, Nos 1/2 and 1989, A285, Nos 1/2/3.
7. M. W. Poole, G. Saxon, D. J. Thompson, "Proposal for a FEL Experiment (FELIX)," Daresbury 1979.
8. A. M. Kondratenko, E. L. Saldin, SOV. PHYS. DOKL., 1979, 24, No 4, 986-990.
9. V. N. Baier, A. I. Mil'shtein, SOV. PHYS. DOKL., 1980, 25, No 6, 112-116.
10. G. Dattoli, T. Letardi, J. M. J. Madey, A. Renieri, NUCL. INSTRUM. & METH., 1985, A237, Nos 1/2, 326-334.
11. G. Dattoli, A. Renieri, NUOVO CIMENTO, 1981, 61F, No 2, 153-180.
12. G. Dattoli, T. Letardi, J. M. J. Madey, A. Renieri, IEEE J. QUANTUM ELECTRON., 1984, QE-20, No 6 (Jun), 637-646.
13. T. Y. Chang, T. J. Bridges, OPT. COMMUN., 1970, 1, 423-426.
14. J. C. Macgillivray, M. S. Feld, CONTEMPORARY PHYS., 1981, 22, 299.
15. F. R. Petersen, et al., IEEE J. QUANTUM ELECTRON., 1975, QE-11, No 10 (Oct), 838-844.
16. K. D. Moller, W. G. Rothschild, "Far Infrared Spectroscopy," Wiley-Interscience, (N. Y. 1971).
17. M. Inguscio, PHYS. SCRIPTA, 1988, 37, No 5, 699-708.
18. E. S. Fu, et al., CHINESE PHYS. LASERS, 1988, 15, No 9 (Sep), 648-650.

- END -

NTIS
ATTN PROCESS 103

5285 PORT ROYAL RD
SPRINGFIELD VA

22161

This is a U.S. Government publication. Its contents in no way represent the policies, views, or attitudes of the U.S. Government. Users of this publication may cite FBIS or JPRS provided they do so in a manner clearly identifying them as the secondary source.

Foreign Broadcast Information Service (FBIS) and Joint Publications Research Service (JPRS) publications contain political, military, economic, environmental, and sociological news, commentary, and other information, as well as scientific and technical data and reports. All information has been obtained from foreign radio and television broadcasts, news agency transmissions, newspapers, books, and periodicals. Items generally are processed from the first or best available sources. It should not be inferred that they have been disseminated only in the medium, in the language, or to the area indicated. Items from foreign language sources are translated; those from English-language sources are transcribed. Except for excluding certain diacritics, FBIS renders personal and place-names in accordance with the romanization systems approved for U.S. Government publications by the U.S. Board of Geographic Names.

Headlines, editorial reports, and material enclosed in brackets [] are supplied by FBIS/JPRS. Processing indicators such as [Text] or [Excerpts] in the first line of each item indicate how the information was processed from the original. Unfamiliar names rendered phonetically are enclosed in parentheses. Words or names preceded by a question mark and enclosed in parentheses were not clear from the original source but have been supplied as appropriate to the context. Other unattributed parenthetical notes within the body of an item originate with the source. Times within items are as given by the source. Passages in boldface or italics are as published.

SUBSCRIPTION/PROCUREMENT INFORMATION

The FBIS DAILY REPORT contains current news and information and is published Monday through Friday in eight volumes: China, East Europe, Soviet Union, East Asia, Near East & South Asia, Sub-Saharan Africa, Latin America, and West Europe. Supplements to the DAILY REPORTs may also be available periodically and will be distributed to regular DAILY REPORT subscribers. JPRS publications, which include approximately 50 regional, worldwide, and topical reports, generally contain less time-sensitive information and are published periodically.

Current DAILY REPORTs and JPRS publications are listed in *Government Reports Announcements* issued semimonthly by the National Technical Information Service (NTIS), 5285 Port Royal Road, Springfield, Virginia 22161 and the *Monthly Catalog of U.S. Government Publications* issued by the Superintendent of Documents, U.S. Government Printing Office, Washington, D.C. 20402.

The public may subscribe to either hardcover or microfiche versions of the DAILY REPORTs and JPRS publications through NTIS at the above address or by calling (703) 487-4630. Subscription rates will be

provided by NTIS upon request. Subscriptions are available outside the United States from NTIS or appointed foreign dealers. New subscribers should expect a 30-day delay in receipt of the first issue.

U.S. Government offices may obtain subscriptions to the DAILY REPORTs or JPRS publications (hardcover or microfiche) at no charge through their sponsoring organizations. For additional information or assistance, call FBIS, (202) 338-6735, or write to P.O. Box 2604, Washington, D.C. 20013. Department of Defense consumers are required to submit requests through appropriate command validation channels to DIA, RTS-2C, Washington, D.C. 20301. (Telephone: (202) 373-3771, Autovon: 243-3771.)

Back issues or single copies of the DAILY REPORTs and JPRS publications are not available. Both the DAILY REPORTs and the JPRS publications are on file for public reference at the Library of Congress and at many Federal Depository Libraries. Reference copies may also be seen at many public and university libraries throughout the United States.